JGR Solid Earth

RESEARCH ARTICLE
10.1029/2019JB018208

Magma Intrusion and Volatile Ascent Beneath Norris Geyser Basin, Yellowstone National Park

C. W. Wicks[1], D. Dzurisin[2], J. B. Lowenstern[2], and J. Svarc[1]

[1]U. S. Geological Survey, Moffett Field, CA, USA, [2]David A. Johnston Cascades Volcano Observatory, U. S. Geological Survey, Vancouver, WA, USA

Key Points:
- Two recent deformation episodes beneath Norris Geyser Basin appear to result from accumulation of magma-derived volatiles at 2–3 km depth
- Volatiles accumulating beneath Norris Geyser Basin could be from magma emplaced from 1996–2001 ~14 km depth beneath the north caldera rim
- Eruptions of Steamboat Geyser and an increased risk of hydrothermal explosions are likely related to the recent deformation episodes

Supporting Information:
- Supporting Information S1

Correspondence to:
C. W. Wicks, and D. Dzurisin,
cwicks@usgs.gov;
dzurisin@usgs.gov

Citation:
Wicks, C. W., Dzurisin, D., Lowenstern, J. B., & Svarc, J. (2020). Magma intrusion and volatile ascent beneath Norris Geyser Basin, Yellowstone National Park. *Journal of Geophysical Research: Solid Earth*, *125*, e2019JB018208. https://doi.org/10.1029/2019JB018208

Received 14 JUN 2019
Accepted 26 JAN 2020
Accepted article online 28 JAN 2020

Abstract Recent activity has provided new insights into the causes of surface deformation in and around the Yellowstone Caldera, a topic that has been debated since the discovery of caldera floor uplift more than four decades ago. An episode of unusually rapid uplift (>15 cm/yr) centered near Norris Geyser Basin along the north caldera rim began in late 2013 and continued until a M_w 4.9 earthquake on 30 March 2014; thereafter, uplift abruptly switched to subsidence. Uplift at rates of several centimeters per year resumed in 2016 and continued at least through the end of 2018. Modeling of Global Positioning System and interferometric synthetic aperture radar data suggests an evolving process of deep magma intrusion during 1996–2001 followed by volatile ascent and accumulation at shallow levels, perhaps as shallow as a few hundred meters depth. The depth of shallow volatile accumulation appears to have shallowed from the 2014 to the 2016 deformation episode, and frequent eruptions of Steamboat Geyser since March 2018 are likely a surface manifestation of this ongoing process. Hydrothermal explosion features are prominent in the Norris Geyser Basin area, and the apparent shallow nature of the volatile accumulation implies an increased risk of hydrothermal explosions.

Plain Language Summary Two recent uplift episodes, from 2013–2014 and 2016 to present, at Norris Geyser Basin in Yellowstone National Park appear to be related to a magma intrusion event during 1996–2001. The uplift probably results from fluids that have been expelled from the intruded magma. The expelled fluids have accumulated at a shallow depth (most likely 2–3 km), and the record number of eruptions of Steamboat Geyser since March 2018 are probably related to the resulting uplift. The shallow nature of the magma-derived fluid accumulation may represent an increased risk of hydrothermal explosions at and around Norris Geyser Basin.

1. Introduction

The volcanic landscape in Yellowstone National Park has been shaped by three very large explosive eruptions within the past 2.1 Myr, each orders of magnitude larger than the largest eruptions anywhere on Earth during historical time. The 75-km by 45-km Yellowstone Caldera formed during the most recent of these eruptions about 631 ka (Christiansen, 2001; Matthews et al., 2015). The caldera hosts two resurgent domes, the Sour Creek dome and Mallard Lake dome (Figure 1), and it is largely filled by rhyolite lava flows that range in age from shortly after caldera formation to as young as 70 ka (Christiansen, 2001; Morgan et al., 2017). Today the Yellowstone Caldera is among the world's most active in terms of seismicity, thermal features, gas emissions, and surface deformation. Leveling surveys in 1923 and 1975–1977 (two complete surveys, the latter spanning three summers) detected uplift of the central caldera floor at an average rate of 14 ± 1 mm/yr (Pelton & Smith, 1979, 1982). Since then, geodetic measurements that now include semi-permanent Global Positioning System (GPS) (Dzurisin et al., 2017), continuous GPS, and interferometric synthetic aperture radar (InSAR) have shown the entire caldera floor to be mobile in space and time (Dzurisin et al., 2012).

Twenty years after the discovery of caldera floor uplift, the first of several secondary deformation sources under the north caldera rim near Norris Geyser Basin (NGB; Figures 1 and 2a) was identified. The deformation near NGB straddled the caldera rim in a pattern distinct from that of coeval deformation of the caldera floor. Since then, both the north rim area and caldera floor have experienced multiple deformation episodes. Modeling reported in this paper identified several sources for north rim deformation, which we refer to as NRUA (North Rim Uplift Anomaly) sources. GPS and InSAR observations from 1996 to 2001 revealed a

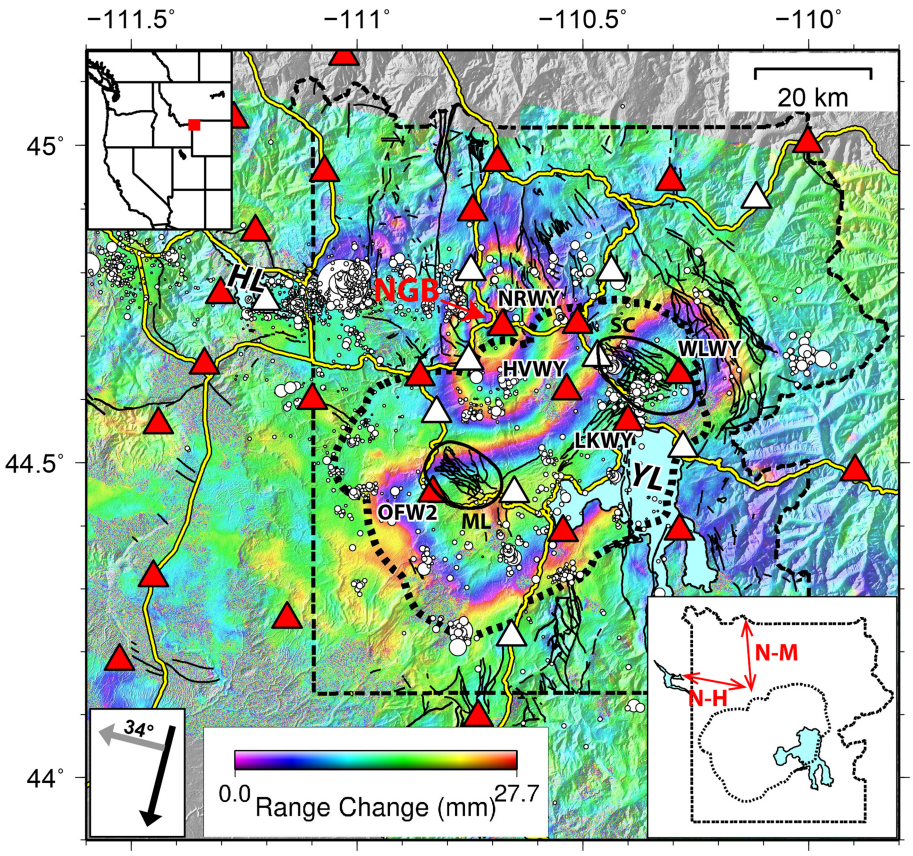

Figure 1. Information map for Yellowstone. The location of Yellowstone is shown with the red square in the regional inset map of the western United States in the top left. A Sentinel 1 interferogram (spanning 9 June 2015 to 4 July 2017) is draped over the 1 arc-sec SRTM DEM (Farr et al., 2007) with a color bar showing the sense of range change in the bottom, the flight path of the satellite (black arrow), and the look direction of the radar instrument (gray arrow with labeled incidence angle of the radar beam with respect to vertical). The boundary of Yellowstone National Park is shown with a bold double-dash black line, and the caldera rim is shown with a bold short single-dash black line. Note that in this paper we use the term "caldera rim" to denote the mapped/estimated outermost collapse scarp. Mapped and inferred faults are shown with thinner black lines, and seismicity during the span of the interferogram is depicted with white-filled black circles. Circle size is scaled to earthquake magnitude which ranges from −0.85 to 4.36. The local highway network in and around Yellowstone is shown with yellow-over-black lines. Two of the larger lakes in the area are labeled HL for Hebgen Lake and YL for Yellowstone Lake. Continuous GPS stations operated by UNAVCO are shown with red-filled black triangles, and five of the continuous GPS stations important for discussion are labeled. Semipermanent GPS stations (Dzurisin et al., 2017) operated by the USGS are shown with white-filled black triangles. The location of Norris Geyser Basin is shown with the red arrow labeled "NGB". The two solid black elliptical polygons labeled "ML" and "SC" show Mallard Lake dome and Sour Creek dome, respectively. The inset map in the bottom right shows the locations of the Norris-Hebgen seismic belt (labeled N-H) and the Norris-Mammoth corridor (labeled N-M)

broad area of uplift centered near the caldera rim and NGB (Meertens et al., 2000; Wicks et al., 2006). In addition to uplift of the caldera floor between 1923 and 1977, Pelton and Smith (1979, 1982) identified an area of relative subsidence at the NRUA location. That NRUA deformation episode might have been akin to subsequent episodes reported here, but it is also possible that it was related to a *M*6.1 earthquake in the area on 30 June 1975 (Pitt et al., 1979). Leveling surveys in 1923 and 1975–1977 measured only net vertical surface displacements during the interval between surveys; hence, the finer timing of caldera floor uplift and north rim relative subsidence is unknown. NGB and the NRUA locations are near the intersection of the Norris-Mammoth corridor and an east-west trending zone of seismicity called the Norris-Hebgen seismic belt (White et al., 1988). The Norris-Mammoth corridor extends north from the north caldera rim, through NGB, to just north of the Park boundary (Christiansen, 2001; Figure 1). The corridor is defined by active normal faults, high seismicity, active thermal features, and postcaldera

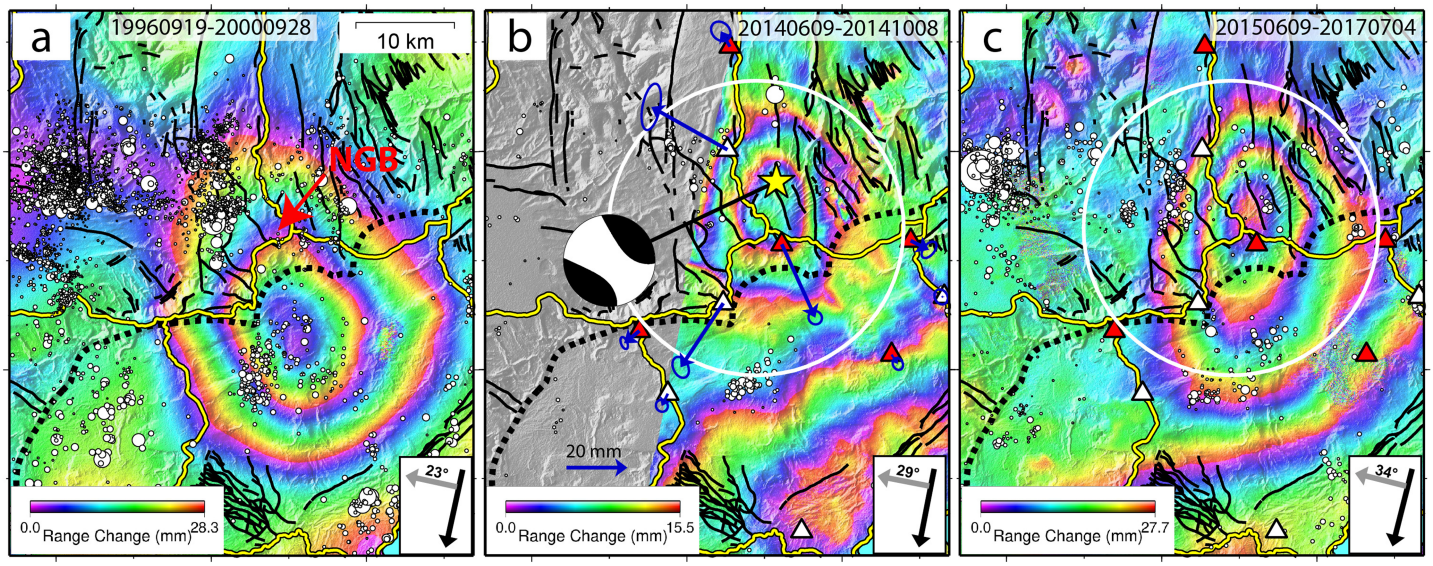

Figure 2. Three descending interferograms that show snapshots of three deformation episodes near the north caldera rim. The description of most features is the same as in Figure 1. Large white circle in (b) and (c) is a 15-km radius circle centered on Norris Geyser Basin (important for Figure 3). (a) ERS2 interferogram spanning 19 September 1996 to 28 September 2000. The red arrow labeled "NGB" shows the location of Norris Geyser Basin. (b) TerraSAR-X interferogram spanning 9 June 2014 to 8 October 2014. Yellow star shows epicenter of M_w 4.9 earthquake that occurred on 30 March 2014. Also shown is a Global Centroid-Moment-Tensor (CMT) solution for the earthquake (Dziewonski et al., 1981, Ekström et al., 2012; http://www.globalcmt.org). Blue arrows (with 95% error ellipses) show peak horizontal surface displacements from GPS from mid-June 2013 to the week after the 30 March 2014 earthquake. A reference vector 20 mm long is in lower left. (c) A Sentinel 1 interferogram spanning 9 June 2015 to 4 July 2017.

eruptions. The Norris-Hebgen seismic belt is a rift-like zone of NNE-SSW extension (Savage et al., 1993; Waite & Smith, 2004) that is a site of minor postcaldera volcanism (Christiansen, 2001; Morgan et al., 2017). The belt extends west from near NGB to the site of the 1959 M_s (surface wave magnitude) 7.5 Hebgen Lake earthquake (a few kilometers north of Hebgen Lake; Figure 1), and it is the zone of densest seismicity within the Park (Waite & Smith, 2002).

Movement of magma, magma-derived volatiles, and hydrothermal fluids are all possible causes for deformation of the caldera floor and NRUA. To produce the massive surface fluxes of CO_2 (Werner & Brantley, 2003) and heat at Yellowstone, the intrusion rate of basaltic magma is required to be about 0.3 km^3/yr (Lowenstern & Hurwitz, 2008). Much of the shallow subsurface (to 4 km depth) in parts of Yellowstone is likely to be vapor saturated with CO_2, which could produce a deformation signal through gas compressibility and mobility. Accumulation of hydrothermal fluids beneath a self-sealing cap and subsequent rupture of the cap with attendant fluid loss is another potential deformation mechanism (Fournier, 1999, 2007), hence the longstanding debate regarding cause(s) of surface deformation.

We present observations and source modeling of three recent NRUA deformation episodes (Figures 2 and 3). The first lasted from about 1996 to 2006, with uplift from 1996 to 2001 (Figure 2a) and mostly subsidence from 2004 to 2006 (and through mid-2013 at a much lower rate; see Figure 3, NRWY). For ease of discussion, we refer to this as the 2000 episode. The second episode (we refer to as the 2014 episode) began with rapid uplift in late 2013 and switched to rapid subsidence after a M_w 4.9 earthquake on 30 March 2014; by early 2015 the subsidence rate had returned to a much lower, long-term rate (Figure 3, NRWY). The earthquake occurred very near the center of NRUA uplift/subsidence (Figure 2b) at a depth of ~7.9 km. A third deformation episode (we refer to as the 2016 episode) began in the winter of 2015–2016 (Figure 3, NRWY) and continued at least through 2018 at a lower rate than during the 2014 episode (3–4 vs. 15–20 cm/yr, respectively). The deformation patterns observable from InSAR for the 2014 and 2016 episodes are similar in the north but different in the south (Figures 2b and 2c), which has implications for models of magma-derived volatile mobility (see section 4). We demonstrate through modeling GPS and InSAR data possible relationships between the three deformation episodes. Complexity of the events in both space and time (three episodes, two with uplift followed by subsidence, plus simultaneous deformation of the adjacent caldera floor)

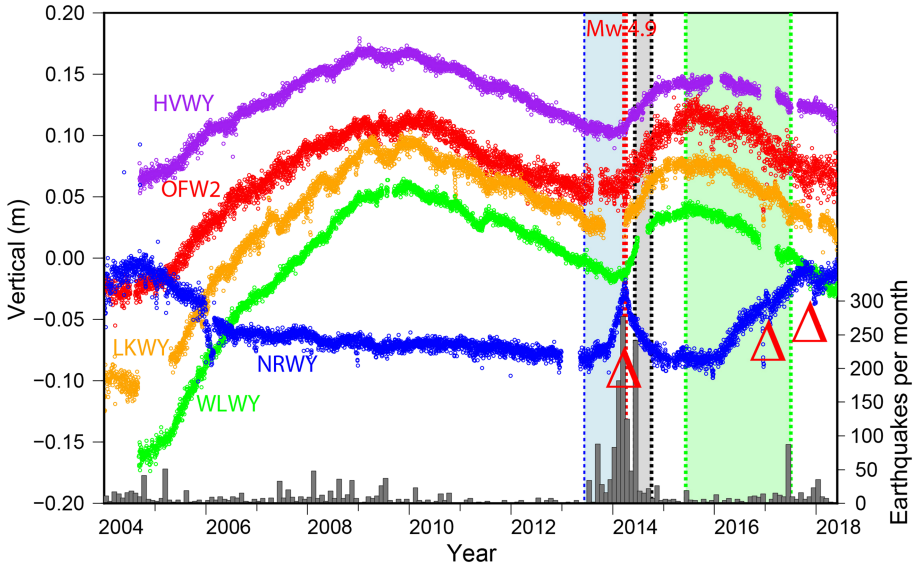

Figure 3. Time series of vertical surface displacements (left axis, arbitrary 0) and monthly numbers of earthquakes (right axis, histogram at bottom) within the caldera and near Norris Geyser Basin from 1 January 2004 to 1 June 2018. Earthquakes are those that fall within the white circle in Figures 2b and 2c. Small colored circles show daily solutions for five labeled GPS stations in Figure 1. These stations were originally installed and operated by the University of Utah Seismograph Stations and have longer time series than other GPS stations in Yellowstone. The time of the M_w 4.9 earthquake is marked by the vertical red dashed line (labeled M_w 4.9). The time interval spanned by GPS measurements in Figure 2b is delimited by the blue rectangular area, the time spanned by the interferogram in Figure 2b is delimited by the gray rectangular area, and the time spanned by the interferogram in Figure 2c is delimited by the green rectangular area. Three red triangles below the time series for NRWY mark significant short-term reversals in uplift.

required a correspondingly detailed modeling effort involving multiple sources and source-types to arrive at our preferred interpretation. Our modeling results are nonunique, but they inform an intuitive narrative that successfully explains more than two decades of deformation at NRUA and the Yellowstone Caldera.

2. Methods

We processed synthetic aperture radar images from various satellites into differential interferograms using the SRTM DEM (Farr et al., 2007) to remove topographic phase. We then filtered the interferograms, unwrapped them, converted them to line-of-sight displacement, and reduced the number of data points using the quadtree windowing method (Jónsson et al., 2002) and a model-based windowing scheme (Lohman & Simons, 2005; Wicks et al., 2013). The method used to find the minimum number of data points necessary to represent the deformation field in an interferogram is given in more detail in Wicks et al. (2013). For modeling purposes, we selected GPS data that span 9 or 10 days on either side of the beginning and ending dates of each interferogram and calculated net surface displacements at each GPS station during each of those intervals. Interferograms derived from synthetic aperture radar scenes acquired near the time of peak uplift in late March 2014 are not coherent because of abundant snow cover, so for intervals starting or ending near the peak uplift we modeled GPS data alone

To model the GPS and InSAR deformation fields, we used a variety of analytic sources and Monte Carlo starting models in nonlinear inversions. Because the deformation patterns in multiple interferograms that span different time intervals within a given NRUA deformation episode are similar in extent, we assumed the deformation source for each time interval, represented by the InSAR and GPS data within an episode, is a scaled version of a reference source that is unique for each NRUA deformation episode. Similarly, we assumed the caldera deformation sources for each episode are scaled versions of a reference source.

In all inversions, we represented the caldera deformation source as a distribution of rectangular dislocations (RDs) (Okada, 1985) made up of two superposed 2-D Weibull distributions (Brodtkorb et al., 2000; Myrhaug & Rue, 1998) on a horizontal plane in an elastic half space. Every 2-D Weibull distribution includes a

covariance (or interaction) parameter (Myrhaug & Rue, 1998) in the inversions, and every 2-D Weibull distribution of opening (or closing) includes a truncation parameter in the inversions that allows none, some, or all of the distribution to be of uniform opening (or closing). The parameters that describe each of the Weibull distributions of RDs were optimized for the caldera deformation source. 2-D Weibull distributions encompass a wide variety of shapes and are well behaved in a nonlinear inversion. 2-D Weibull distributions of dislocation models have been used previously to model earthquake ruptures (Wicks et al., 2013), volcanic sources (Wicks et al., 2011), and mine collapse (Lu & Wicks, 2010). In addition to the model parameters, a static shift parameter is found for each interferogram in the inversions. In all of the inversions we also weighted each GPS directional component and each InSAR quadtree point by the inverse of the one sigma value associated with the measurement.

Because of the greater sensitivity of GPS data to source geometry (Dieterich & Decker, 1975) and to gain some insight into the required modeling, we first modeled only the GPS data. As alternative models of the data for a NRUA deformation source, we tested volumetric sources, a tabular source, and a dome-shaped reservoir. The volumetric sources are a prolate spheroid (Yang et al., 1988) and a compound dislocation model (CDM, Nikkhoo et al., 2017). The tabular body is a sill-like body composed of a distribution of RDs (or triangular dislocations [TDs]; Nikkhoo & Walter, 2015) where the distributed opening (or closing) is described by a 2-D Weibull dislocation. The dome-shaped deformation source is a distribution of TDs where the depth variation is described by one 2-D Weibull distribution and the amount of opening or closing is described by another.

We used *F* tests and 95% probability to determine which competing models are acceptable and to determine uncertainty intervals. The quadtree parsed data for one interferogram can be treated as independent data points (Jónsson, 2002), allowing us to use *F* tests. However, we have multiple interferograms for each deformation episode, and because we assumed the sources for each time interval spanned by an interferogram are a scaled version of a reference source, we did not use the full number of quadtree InSAR data points in estimating the number of degrees of freedom. Instead we estimated the number of data points needed to represent a single descending interferogram and a single ascending interferogram for each episode. This gave us a good-faith estimate of the number of degrees of freedom and slightly more conservative (broader) estimates of uncertainties and what defines an acceptable model.

3. Data and Modeling Results

Data for the 2014 episode consist of seven interferograms (six from TerraSAR-X and one from RADARSAT-2, supporting information Figures S1–S7) and three discrete surface displacement measurements from continuous and semipermanent (Dzurisin et al., 2017) GPS stations covering different parts of the uplift/subsidence cycle (Figures S8–S10). We found the model that best fit only the GPS data was a dome-shaped reservoir. The flat-lying, sill-like body of distributed RDs, RDs, or TDs provided the next best fit, and the prolate spheroid and CDM sources provided the worst fit. We found both the dome-shaped and flat-lying sources to be acceptable (or insignificantly different), whereas the prolate spheroid and CDM sources are unacceptable.

By extending the modeling to include the seven interferograms, we found a dome-shaped model fit the data best; however, the GPS data were systematically misfit by the best fit minimum variance model. By applying a weighting of 10 to the GPS data we fit the GPS data within two-sigma uncertainty, but the misfit to the InSAR data was significantly greater. We then reduced the GPS weighting systematically until, with a weighting of 4, the InSAR misfit was insignificant compared to the unweighted best fit. The resulting dome model is shown in Figures 4a–4c and in more expansive view in Figure S11. The resulting data misfit is shown in Figures S8–S10, S12, and S13. The TDs shown in the NRUA source reflect the maximum amount of opening consistent with the GPS data shown in Figures 2b and S10, which corresponds to a volume change of ~0.02 km^3. The distributed RDs beneath the caldera (Figure S11) represent the source with the maximum uplift measured by caldera GPS stations from April 2014 to August 2015 (Figure S8).

For the 2016 episode, the data consist of six interferograms (one TerraSAR-X, one ALOS2, and four Sentinel 1; Figures S14–S19) and one set of discrete displacement measurements from continuous and semipermanent GPS stations (Figure S20). In the same approach as used to model the 2014 episode, we first modeled the GPS data alone (Figure S20) with a variety of sources. We found that for the NRUA source, the CDM

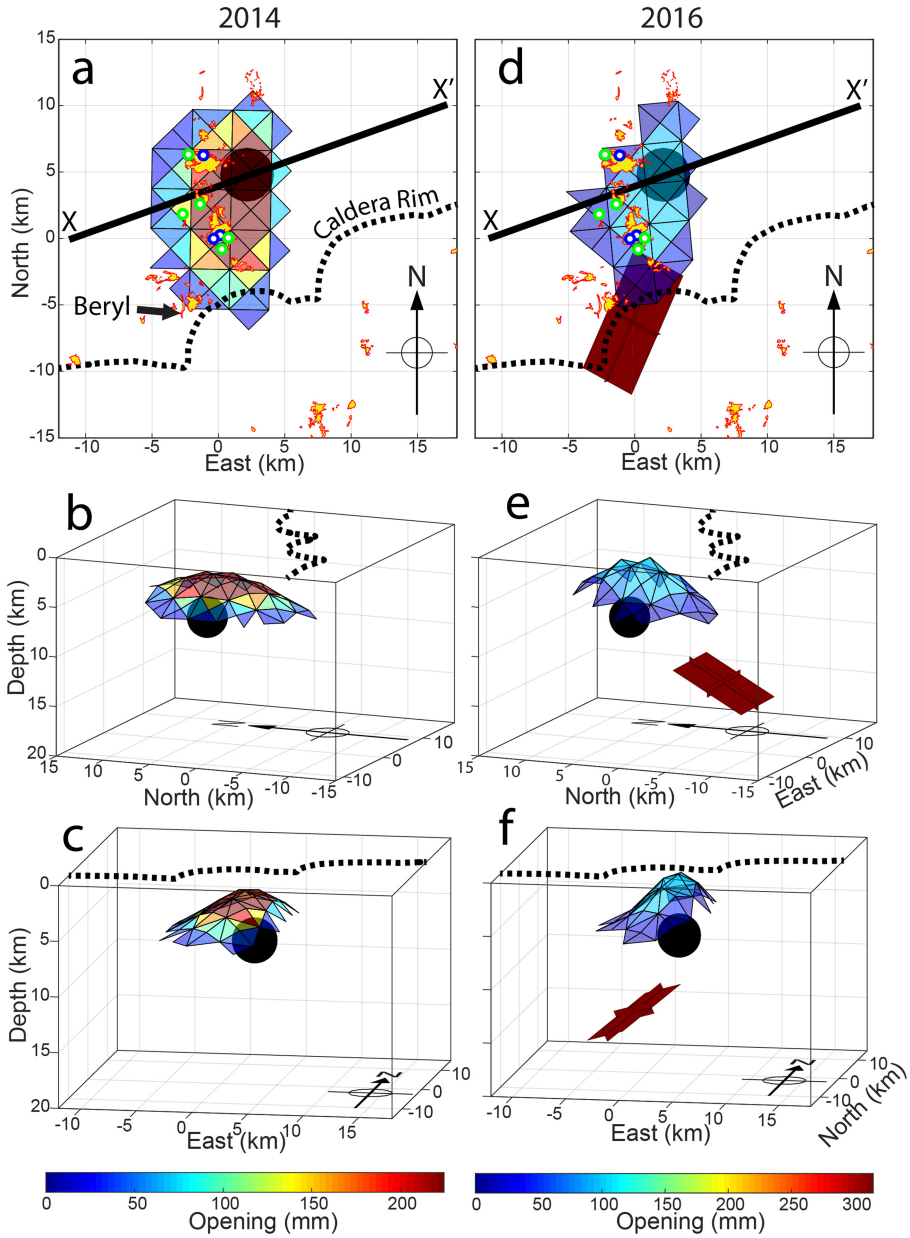

Figure 4. Comparison of modeled NRUA deformation sources for the 2014 (left column) and 2016 (right column) episodes. The origin for the east, north coordinates is in the center of NGB. To aid in reader orientation, the dashed bold black line in (a)–(f) shows the north caldera rim (as labeled in (a)), the 4-km diameter black sphere shows the location of the 30 March 2014 M_w 4.9 earthquake (Figures 2 and 3), and a north arrow is shown in the SE corner of each panel. The plan views in (a) and (d) show the mapped active thermal areas (Christiansen et al., 2007) as yellow areas with a red outline. Mapped historic hydrothermal explosions (Christiansen et al., 2007) are shown as green circles. Mapped hydrothermal explosion craters greater than 100 m diameter (Christiansen et al., 2007) are shown as blue circles. (a) Plan view of the 2014 deformation source. Arrow labelled "Beryl" shows location of Beryl Spring (see section 4). Bold black line labeled X-X′ shows location of cross section in Figure 6. (b) Perspective view of 2014 source viewed from WSW. (c) Perspective view of 2014 source from SSE. (d) Plan view of 2016 deformation sources. (d) Perspective view of 2016 sources from WSW. (f) Perspective view of 2016 sources from SSE.

and dome-like distribution of TDs fit the data best, whereas the prolate spheroid and flat-lying sill-like body of distributed TDs fit the data worst. We then extended the modeling to include the interferograms; the resulting best fit model, which required two sources, is shown in Figures 4d–4f, and in a more expansive

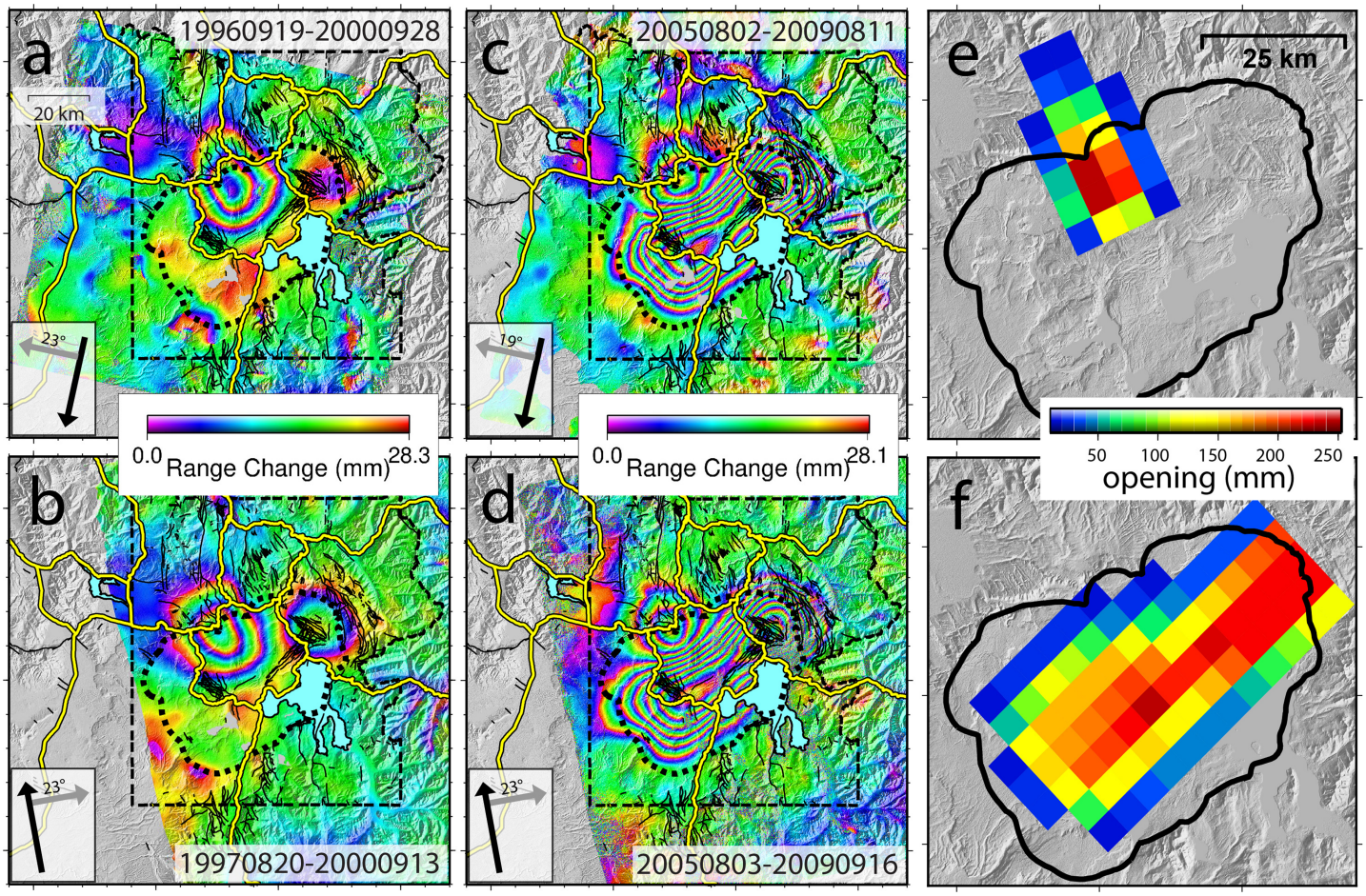

Figure 5. InSAR data used in modeling and resulting source models for 2000 NRUA episode. Features are as described in Figure 1. Color bars show the range change for one fringe. Black arrows in (a)–(d) show satellite flight direction, and gray arrows show radar look direction, labeled with radar incidence angle. (a) ERS-2 descending interferogram from 19 September 1996 to 28 September 2000. (b) ERS-2 ascending interferogram from 20 August 1997 to 13 September 2000. (c) ENVISAT descending interferogram from 2 August 2005 to 11 August 2009. (d) ENVISAT ascending interferogram from 3 August 2005 to 16 September 2009. (e) Distribution of RDs representing the NRUA uplift source for the 2000 episode spanned in Figure 5a. (f) Uplift source for the caldera from 2005 to 2009 in Figures 5c and 5d.

view in Figure S21. The resulting data misfit is shown in Figures S20, S22, and S23. Using the same approach described above for the 2014 episode, we arrived at a weighting factor of 5 for the GPS data in this case. The best fitting shallow, domed reservoir for the 2016 episode is similar in extent to that obtained for the 2014 episode but somewhat shallower. The top of the domed model in the 2014 episode (Figures 4a–4c) is about 3.2 km depth, whereas the top of the domed model in the 2016 episode (Figures 4d–4f) is about 1.8 km depth. The main difference between models for the two episodes is that an additional body is needed for the 2016 episode to account for its broader deformation field south of the caldera rim. The additional source is the deep dipping tabular CDM source shown in Figures 4d–4f and S21.

Because a flat-lying sill-like distribution of RDs (or TDs) provided an acceptable fit to the GPS data for the 2014 episode (although not as good as a dome-shaped source model), we also modeled the GPS plus InSAR data with such a source model. We could not get an acceptable fit to the combined dataset using only a sill-like source. However, by adding an additional RD source to the inversion, we arrived at an acceptable model that we show in Figures S24a–S24c and S25. The model is plausible, but the added complexity lends favor to the simpler dome-shaped model (Figures 4a–4c).

We also modeled GPS plus InSAR data for the 2016 episode with a flat-lying sill-like deformation source; results are shown in Figures S24d–S24f and S25. The resulting residuals are not significantly different

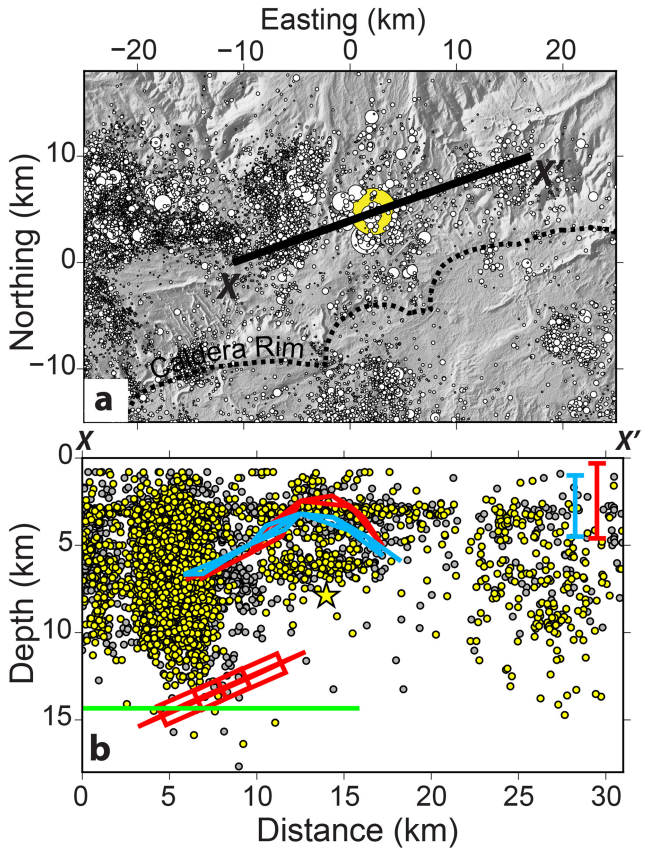

Figure 6. Location map, epicenters, and cross section of seismicity through NGB. (a) Location map and epicenters for the last 25 years of seismicity recorded by the University of Utah Seismograph Stations. White-filled circles mark locations of earthquakes scaled to earthquake magnitude ranging from −0.99 to 4.9. The yellow-filled circle marks the location of the M_w 4.9 30 March 2014 earthquake. Heavy dashed line shows the Yellowstone Caldera rim (as labeled). Solid bold black line labeled X-X′ shows location of the cross section in (b). (b) Depth cross section through X-X′ showing the NRUA sources in Figure 4. Gray-filled circles show earthquakes from (a) within 4 km of distance normal to the vertical plane through X-X′; yellow-filled circles represent earthquakes within 2 km distance of X-X′. The catalog hypocenter depths are shifted to represent depth beneath the surface at NGB. The projected location of the 30 March 2014 M_w 4.9 earthquake (Figures 2 and 3) is shown with the yellow-filled black star. The shallow blue lines are the projected part of the source for the 2014 deformation episode (Figures 4a–4c) beneath NGB within 2 km of X-X′. The shallow red lines are the projected part of the shallow source of the 2016 episode (Figures 4d–4f) within 2 km of X-X′. The deeper red lines are the projected CDM component for the deeper 2016 source (Figures 4d–4f). The green line is the projected NRUA deformation source for the 2000 deformation episode (Figures 6e, S21, and S24d–S24f). Blue and red "error bars" in the upper right represent estimates of the possible range of depths to the top of the shallowest part of the 2014 and 2016 deformation source models, respectively.

from those for the model shown in Figures 4d–4f. In this model, the flat-lying sill-like body extends about 20 km across the north caldera rim, into the center of the caldera.

To compare modeled deformation sources from all three recent NRUA uplift episodes, we assumed flat-lying distributions of RDs for the 2000 episode. Using the same methods as for the 2014 and 2016 episodes, we found sources beneath the caldera and NRUA by modeling the four interferograms shown in Figure 5. There are two interferograms, one ascending and one descending, that recorded the uplift portion of the 2000 NRUA episode (Figures 5a and 5b) and there are two interferograms, one ascending and one descending, that recorded the subsidence portion (Figures 5c and 5d). The first two interferograms cover different time intervals whereas the latter two cover essentially (for modeling purposes) the same time interval. We used 2-D Weibull distributed RDs to represent the deformation sources beneath both NRUA and the caldera in all four interferograms. Competition between simultaneous uplift of the caldera and subsidence of the NRUA area introduces an additional degree of non-uniqueness to the problem.

To address this source competition problem, we first found a reference NRUA source that fits the two interferograms in Figures 5a and 5b that exhibit inflation at NRUA. In these two interferograms the caldera deformation field is minimal (i.e., not encroaching on the NRUA deformation signal very much). The reference NRUA deformation source (Figure 5e) fits the interferogram in Figure 5a, and the source for the interferogram in Figure 5b is a scaled version of this reference source. We then inverted for deformation sources for all four interferograms in Figures 5a–5d where the NRUA sources are forced to be scaled versions of the reference source in Figure 5e and scaled versions of a reference caldera source that was determined in the inversion and consisted of two superposed 2-D Weibull distributions. We optimized the parameters that described each of the two Weibull distributions, but constrained them to lie on the same plane. The reference caldera source (Figure 5f) fits the two interferograms in Figures 5c and 5d. The fit to the data is shown in Figures S26 and S27.

The caldera deformation source model (Figure 5f) depth is ~6 km, consistent with the depth (5–8 km) to caldera sources during the 2014 and 2016 NRUA episodes, whereas the depth of the NRUA source is ~14 km, much deeper than the NRUA sources for the 2014 and 2016 episodes. Depths for caldera deformation sources from other studies vary from ~4 to 20 km depth (Tizzani et al., 2015; and references therein). Other studies of the 2000 NRUA episode (tabulated in Tizzani et al., 2015) have found the depth of the NRUA source to be between ~7 and 20 km. The bottom of the CDM components for the NRUA deformation sources from the 2016 episode appear to intersect (or nearly intersect) the NRUA source for the 2000 episode (Figures 6, S21, and S24, and S25). Previous studies suspected the geometry of the NRUA deformation source model changed from the uplift portion of the episode to the subsidence portion (Tizzani et al., 2015; Vasco et al., 2007), but our modeling shows this is not a necessary condition.

One of the most important aspects of this study, particularly as it relates to hazards such as hydrothermal explosions, is an estimate of the depth to the top of shallowest part of the deformation source models beneath NRUA. By repeatedly fixing the depth to the top of the dome at different depths with all other model parameters allowed to vary in multiple inversions, we were able to estimate the uncertainty of the depth to the top of the domes for the 2014 episode. We found that the depth to the top of the domed deformation

source model for the 2014 episode (Figures 4a–4c) is between 1 and 4.5 km (shown as an error bar in Figure 6 b). Using the same procedure for the 2016 episode, the shallowest acceptable estimate for the top of the domed model component (Figures 4d–4f) is ~0.3 km. Evaluating the deepest estimate to the top of the dome for the 2016 episode is problematic because of tradeoffs between the dome source and the CDM source. As the top of the dome is forced to be deeper it becomes flatter and the CDM source becomes more elongate and shallower. When the dome is totally flat it is a sill at about 6.3 km depth (see section 4 and Figures S24d–S24f), but the shallowest part of the alternate source model in Figures S24d–S24f is 4.6 km to the top of the CDM component. So, we use 0.3 km and 4.6 km as the range of possible depths to the top (shallowest part) of deformation models for the 2016 episode (shown as an error bar in Figure 6b). The distribution of the standard errors for the located depth of the earthquakes in Figure 6b is long tailed with a sharp peak near 1 km. The mean standard error is ~3.3 km, whereas the median is ~1 km.

4. Discussion and Conclusions

The Norris-Mammoth corridor is the only major hydrothermal area in Yellowstone National Park outside the Yellowstone Caldera, and it contains the only mapped hydrothermal explosion features outside the caldera (Christiansen et al., 2007) (Figures 4a, 4d, S24a, and S24d). A detailed study of the geology and thermal features of NGB concluded that one or more magmatic heat sources must exist along the corridor to account for its vigor and longevity (White et al., 1988), and the NRUA area was suggested as an outlet for near continuous basaltic magma flow that rises under the caldera (Wicks et al., 2006). Seismicity in the Norris area is anomalously shallow (Figure 6b), suggesting a local heat source has raised the brittle-ductile transition there to within 5–6 km of the surface (Pitt et al., 1979), nearly as shallow as inferred beneath the central axis of the caldera (~5 km or less, Smith & Braile, 1994).

To inform a conceptual model of the processes responsible for recurring deformation at NRUA, we need to interpret features of the kinematic models in Figures 4, 6, S11, and S21 in a physical context. The domed source shown in Figures 4a–4c can be interpreted as a shallow (~3.2 km depth to the top) accumulation of magmatic volatiles at a domed interface, apparently (from seismicity) within the brittle portion of the crust (Figure 6b). However, two factors add uncertainty to the location of the brittle-ductile boundary as determined from seismicity (Fournier, 1999): (1) Inhomogeneities in the composition of the rock would make the brittle-ductile transition occur over an interval of depth; and (2) High strain rates within the ductile region can cause brittle behavior, thus seismicity. High strain rates can be the result of rapid migration of fluids within the ductile region. The abundant seismicity below the domed sources in Figure 6b would suggest fluids (volatiles) migrate quite often beneath NGB if that process is the cause of observed seismicity.

Based on results of research drilling at Yellowstone and elsewhere, laboratory experiments, and theoretical considerations, it has been proposed that horizontal lenses of fluid derived from an underlying magma body accumulate in a ductile zone (at lithostatic pressure) and below a self-sealed zone that separates the ductile zone from the overlying brittle crust (at hydrostatic pressure; Fournier, 1999). According to the model, at some point an input pulse of fluid initiates a runaway vertical migration of fluids that ruptures the seal, allowing fluid access to the brittle zone.

The domed model for the 2016 uplift (Figures 4d–4f) is shallower than the domed model for the 2014 episode (~1.8 vs. 3.2 km to the top), but a CDM source is also required for the 2016 episode. The tabular CDM source extends from ~15.4 km depth to ~11.1 km depth. Like the domed source for the 2014 episode, the 2016 domed model is for the most part confined to the area north of the caldera rim. The mapped north caldera rim (Christiansen, 2001) is buried but inferred to be south of both models. However, an alternative model for the 2016 episode (Figures S24d–S24f) that fits the deformation data acceptably well has a sill-like deformation source at ~6.3 km depth that extends as much as 20 km across the north rim into the caldera. This model implies a fluid reservoir near 6–7 km depth that is perhaps in direct communication with another such reservoir beneath the caldera. In this alternative model, the CDM source (again required) is more pipe-like, extending from ~13.5 km depth to ~4.6 km depth. The distribution of surface thermal features and hydrothermal explosion features is discontinuous across the north caldera rim, in apparent discord with a shallow reservoir that crosses the north caldera rim (Figure S24d). Also favoring a reservoir restricted to the area north of the north caldera rim is the absence of a continuous band of seismicity across the rim (Figure 6a) above the flat-lying 2016 modeled source (Figure S24d). These observations do not rule out the possibility

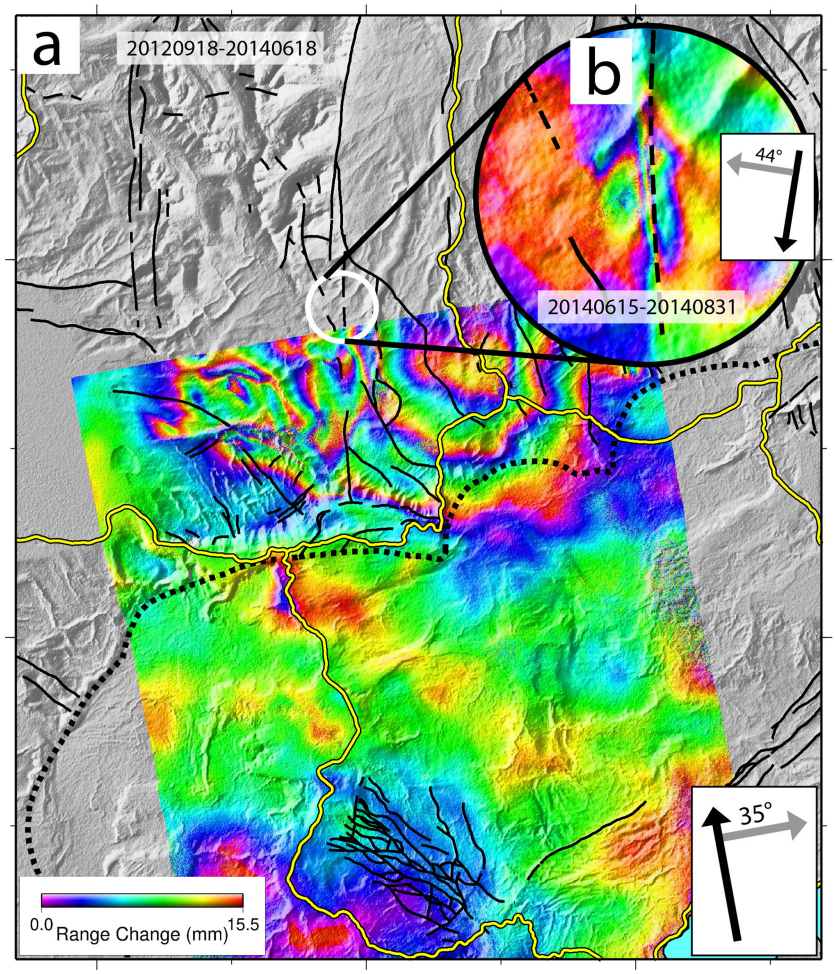

Figure 7. Interferograms showing small-scale deformation features that might result from volatiles escaping to the surface west of NGB after the 30 March 2014 M_w 4.9 earthquake. Black arrows show satellite flight direction, and gray arrows show radar look direction, labeled with radar incidence angle. (a) TerraSAR-X ascending interferogram from 18 September 2012 to 18 June 2014 showing inflation centered near NGB and small-scale (shallower) inflation features west of NGB. The 4 km diameter white circle shows the area covered in the interferogram in (b). Unfortunately, the TerrraSAR-X strip map acquisitions before the 2014 episode were truncated. (b) TerraSAR-X descending interferogram from 15 June 2014 to 31 August 2014 showing a (collapsing) shallow dike-like feature.

that a reservoir breached the caldera rim during the 2016 episode, but they favor the model scenarios in Figure 4, in which the caldera rim is an effective barrier for a shallow domed reservoir beneath NGB.

We infer that the 2014 and 2016 deformation episodes at NRUA were caused by progressive ascent and accumulation of volatiles derived from magma emplaced during the 2000 episode, interrupted temporarily when the expanding volatile reservoir ruptured during the M_w 4.9 30 March 2014 earthquake. The 2000 episode might have been caused by emplacement of magma beneath NRUA by an event that impeded the continuous flow of basalt beneath Yellowstone that is required to maintain the active magmatic and hydrothermal systems (Lowenstern & Hurwitz, 2008; White et al., 1988; Wicks et al., 2006). High $^3He/^4He$ ratios measured at Beryl Spring (Figure 4a), second only to those measured at Mud Volcano near the Sour Creek resurgent dome (Figure 1) (Kennedy et al., 1985), are a good indicator of a basaltic source beneath NRUA (White et al., 1988). However, we do not know if the magmatic intrusion we hypothesize to account for the 2000 deformation episode is basaltic or rhyolitic in nature. Monitoring the composition and flux of volatiles at the surface might be the best way to discriminate between these possibilities (Lowenstern & Hurwitz, 2008). Continuous (or regular) sampling of areas within and west of NGB might capture changes that could be used to investigate the provenance of volatiles related to recent and future deformation events.

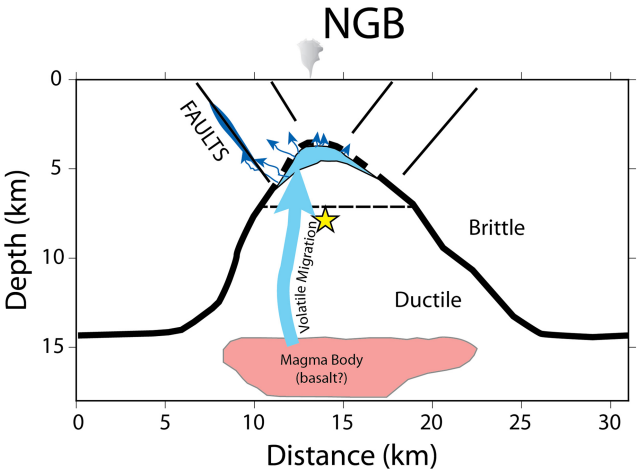

Figure 8. Schematic cross section looking north along the axis of the Norris-Mammoth corridor, showing a model like that described by Fournier (1999) that is responsible for the deformation episodes at NRUA. The yellow star shows the location of the 30 March 2014 M_w 4.9 earthquake. The horizontal dashed line shows the alternate possible depth where volatiles might have accumulated (Figures S24 and S25). The thin black lines depict the network of faults that correspond to the subsidence structure of the Norris-Mammoth corridor.

The interferogram in Figure 7a for the interval from 18 September 2012 to 18 June 2014 shows net uplift at NRUA about 2.5 months after uplift switched to subsidence according to the NRWY GPS record (Figure 3). Our modeling indicates that about half the peak uplift volume was lost between the time of the earthquake (30 March 2014) and the end date of the interferogram (18 June 2014). The same interferogram shows small-scale deformation features west of NGB (Figure 7a). We attribute these features to shallow fluid movement after the 30 March 2014 earthquake and propose the following scenario: Uplift that began in late 2013 was caused by fluid accumulation in a sealed reservoir that ruptured at the time of the 30 March 2014 earthquake, initiating subsidence and volatile migration into the faulted area west of NGB. There are areas in Yellowstone that exhibit a seasonal deformation signal (spring to fall or fall to spring), most likely from filling of the shallow part of highly permeable faults during rapid melting of accumulated snow cover. Some small-scale features in the area west of NGB exhibit this behavior, but the area affected and the amplitude of the features in Figure 7a are anomalously large. In our opinion, they are more likely related to fluids liberated by the 30 March 2014 earthquake that migrated westward and upward along faults and fractures (shown schematically in Figure 8). This area is also the location of a shallow tomographic velocity anomaly interpreted to be caused by CO_2 accumulation (Husen et al., 2004). If the fluids displaced meteoric water in faulted, colder rock west of NGB, we would expect small-scale reversible deformation as the hot fluids cooled—consistent with the interferograms in Figure 7. An inferred fault (Christiansen, 2001; Figure 7b) at the location of a small-scale deformation feature that exhibits in interferograms the deformation field of a contracting dike might be a good location to measure volatiles unmodified by active hydrothermal features, although it is in hard-to-access Yellowstone backcountry that is buried under snow about 6 months of the year.

How unusual are extracaldera deformation episodes at NGB? None prior to the 2000 episode are confirmed by geodetic measurements. However, dilatational strain related to the 2000 episode probably played a role in increased activity of Steamboat Geyser in NGB starting in May 2000 (Wicks et al., 2006). Steamboat erupts with the highest plume of any geyser in the world, and it has gone for long periods (up to 50 years; White et al., 1988) without erupting. In contrast to the 2000 episode, the source of the ongoing 2016 episode is shallower and more concentrated beneath NGB (Figures 4d–4f). Steamboat erupted 32 times in 2018, surpassing its record of 29 eruptions in 1964, and 39 more times by 7 October 2019. If we suppose, as seems likely, that Steamboat is a good natural strainmeter, then its high eruption frequency in the 1960s, early 1980s (White et al., 1988), and 2018–2019 suggests that NRUA deformation episodes occur on decadal timescales. We suspect that deformation, with attendant infusion of magmatic volatiles and heat, is normal at NGB and might even be required to maintain its abundant hydrothermal features.

Hydrothermal explosions are also common in the NGB area (Christiansen et al., 2007) (Figures 4a, 4d, S24a, and S24d), and the risk of such an event probably increases during NRUA uplift episodes like the current one. An intriguing and potentially important aspect of our study from a hazard perspective is the apparent shallowing of the 2016 uplift source relative to the 2014 source, from a top at ~3.2 km in 2014 to ~1.8 km in 2016. Two other temporary reversals in the NRWY GPS time series indicate other possible ruptures in the winters of 2016–2017 and 2017–2018 (red triangles in Figure 3). If, as we believe, expansion and shallowing (possibly to only a few hundred m depth) of the source indicates accumulation and ascent of magmatic volatiles, then additional monitoring and modeling is important to determine if that trend is continuing. Future detailed study of the 2016 episode will hopefully shed more light on this.

From a research perspective, the most salient aspect of our study is that it encompasses the entirety of a process from deep magma intrusion to volatile exsolution, ascent, and accumulation in a shallow, upwardly expanding reservoir. So far, the process has been expressed at the surface by increased activity at Steamboat Geyser and by isolated fluid leaks along faults west of NGB. Each stage in this process has been invoked in earlier studies, including some by the authors of this paper, to explain deformation episodes at

Yellowstone. The result was a succession of papers that proposed magma, hydrothermal fluids, magmatic gases, or some combination as the primary deformation agent. The conceptual model proposed here integrates those ideas. It also raises some questions in need of further investigation. How frequent are discrete magmatic intrusions beneath NRUA and the Yellowstone Caldera? To what extent are magmatic and volatile reservoirs beneath those areas linked? What role do magmatic fluids play in frequent seismic swarms between NRUA and the Hebgen Lake fault zone? What influence does the fault zone have on Yellowstone's magmatic system, and vice versa? What is the most likely outcome of the current NRUA uplift episode? Answers to these questions will not come easily, but their importance should motivate continued vigilance and research at Earth's most dynamic caldera system.

Acknowledgments
James Savage, Fred Pollitz, Evelyn Roeloffs, Luis Lara, and Zhong Lu provided constructive suggestions to improve the manuscript. Peter Cervelli and Mike Lisowski contributed to our thinking about the 2014 deformation episode at Norris Geyser Basin and the effects of the 30 March 2014, M_w 4.9 earthquake. Joel Robinson provided technical assistance. Sentinel 1 data were made available by the European Space Agency. TerraSAR-X data were made available by the Deutsches Zentrum für Luft- und Raumfahrt (DLR) through DLR projects GEO1142 and GEO1742. ALOS-2/PALSAR data are copyright by the Japan Aerospace Exploration Agency (JAXA) and the Japanese Ministry of Economy, Trade and Industry (2015, 2016) and were made available through JAXA project P1216002. Radarsat-2 data were made available by the Canadian Space Agency through MDA Geospatial Services via the COMSAR initiative with the National Geospatial-Intelligence Agency. GPS data used in the study are available at UNAVCO. The authors were fully funded by the USGS for this research. This study complies with FAIR Data standards by providing data that are not obtainable from cited studies. GPS static offsets and InSAR line-of-sight displacement data are available online (https://doi.org/10.6084/m9.figshare.11317817.v1).

References

Brodtkorb, P. A., Johannesson, P., Lindgren, G., Rychlik, I., Rydén, J. & Sjö, E. (2000). WAFO—A Matlab toolbox for analysis of random waves and loads, *Proceedings of the 10th International Offshore and Polar Engineering Conference, 3*, 343-350.

Christiansen, R. L. (2001). The Quaternary and Pliocene Yellowstone plateau volcanic field of Wyoming, Idaho, and Montana. *U. S. Geological Survey Professional Paper 729-G*, 120p, https://pubs.usgs.gov/pp/pp729g.

Christiansen, R. L., Lowenstern, J. B., Smith, R. B., Heasler, H., Morgan, L. A., Nathenson, M., et al. (2007). Preliminary assessment of volcanic and hydrothermal hazards in Yellowstone National Park and vicinity. *U. S. Geological Survey Open-file Report 2007-1071*, 94p, https://pubs.usgs.gov/of/2007/1071.

Dieterich, J. H., & Decker, R. W. (1975). Finite element modeling of surface deformation associated with volcanism. *Journal of Geophysical Research*, *80*, 4094–4102.

Dziewonski, A. M., Chou, T. A., & Woodhouse, J. H. (1981). Determination of earthquake source parameters from waveform data for studies of global and regional seismicity. *Journal of Geophysical Research*, *86*, 2825–2852. https://doi.org/10.1029/JB086iB04p02825

Dzurisin, D., Lisowski, M., & Wicks, C. W. Jr. (2017). Semipermanent GPS (SPGPS) as a volcano monitoring tool: Rationale, method, and applications. *Journal of Volcanology and Geothermal Research*, *344*, 40–51. https://doi.org/10.1016/j.jvolgeores.2017.03.007

Dzurisin, D., Wicks, C. W., & Poland, M. P. (2012). History of surface displacements at the Yellowstone Caldera, Wyoming, from leveling surveys and InSAR observations, 1923-2008. *U. S. Geological Survey Professional Paper 1788*, 68p, https://pubs.usgs.gov/pp/1788/.

Ekström, G., Nettles, M., & Dziewonski, A. M. (2012). The global CMT project 2004–2010: Centroid-moment tensors for 13,017 earthquakes. *Physics of the Earth and Planetary Interiors*, *200-201*, 1–9. https://doi.org/10.1016/j.pepi.2012.04.002

Farr, T. G., Rosen, P. A., Caro, E., Crippen, R., Duren, R., Hensley, S., et al. (2007). The Shuttle Radar Topography Mission. *Reviews of Geophysics*, *45*, RG2004. https://doi.org/10.1029/2005RG000183

Fournier, R. O. (1999). Hydrothermal processes related to movement of fluid from plastic into brittle rock in the magmatic-epithermal environment. *Economic Geology*, *94*, 1193–1212. https://doi.org/10.2113/gsecongeo.94.8.1193

Fournier, R. O. (2007). Hydrothermal systems and volcano geochemistry. In *Volcano deformation—Geodetic monitoring techniques*, (pp. 323–341). Berlin: Springer-Praxis Books.

Husen, S., Smith, R. B., & Waite, G. P. (2004). Evidence for gas and magmatic sources beneath the Yellowstone volcanic field from seismic tomographic imaging. *Journal of Volcanology and Geothermal Research*, *131*, 397–410. https://doi.org/10.1016/S0377-0273(03)00416-5

Jónsson, S. (2002). Modeling volcano and earthquake deformation from satellite radar interferometric observations. PhD thesis, Stanford Univ.

Jónsson, S., Zebker, H., Segall, P., & Amelung, F. (2002). Fault slip distribution of the 1999 M_w 7.1 Hector Mine, California, earthquake, estimated from satellite radar and GPS measurements. *Bulletin of the Seismological Society of America*, *92*, 1377–1389. https://doi.org/10.1785/0120000922

Kennedy, B. M., Lynch, M. A., Reynolds, J. H., & Smith, S. P. (1985). Intensive sampling of noble gases in fluids at Yellowstone: I. Early overview of the data; regional patterns. *Geochimica et Cosmochimica Acta*, *49*, 1251–1261. https://doi.org/10.1016/0016-7037(85)90014-6

Lohman, R. B., & Simons, M. (2005). Some thoughts on the use of InSAR data to constrain models of surface deformation: Noise structure and data downsampling. *Geochemistry, Geophysics, Geosystems*, *6*, Q01007. https://doi.org/10.1029/2004GC000841

Lowenstern, J. B., & Hurwitz, S. (2008). Monitoring a supervolcano in Repose: Heat and volatile flux at the Yellowstone Caldera. *Elements*, *4*, 35–40. https://doi.org/10.2113/GSELEMENTS.4.1.35

Lu, Z., & Wicks, C. Jr. (2010). Characterizing 6 August 2007 Crandall Canyon mine collapse from ALOS PALSAR InSAR. *Geomatics, Natural Hazards and Risk*, *1*, 85–93. https://doi.org/10.1080/19475701003648077

Matthews, N. E., Vazquez, J. A., & Calvert, A. T. (2015). Age of the Lava Creek supereruption and magma chamber assembly at Yellowstone based on $^{40}Ar/^{39}Ar$ and U-Pb dating of sanidine and zircon crystals. *Geochemistry, Geophysics, Geosystems*, *16*, 2508–2528. https://doi.org/10.1002/2015GC005881

Meertens, C. M., Smith, R. B., & Puskas, C. M. (2000). Crustal deformation of the Yellowstone Caldera from campaign and continuous GPS surveys, 1987-2000. *Eos Transactions AGU*, *81*(48). Fall Meeting Supplement, Abstract V22F-19

Morgan, L. A., Shanks, W. C. P., Lowenstern, J. B., Farrell, J. M., & Robinson, J. E. (2017). Geologic field-trip guide to the volcanic and hydrothermal landscape of the Yellowstone Plateau: *U. S. Geological Survey Scientific Investigations Report 2017-5022-P*, 100 p., doi: https://doi.org/10.3133/sir20175022P.

Myrhaug, D., & Rue, H. (1998). Joint distribution of successive wave periods revisited. *Journal of Ship Research*, *42*, 199–206.

Nikkhoo, M., & Walter, T. R. (2015). Triangular dislocation: An analytical, artefact-free solution. *Geophysical Journal International*, *201*, 1119–1141. https://doi.org/10.1093/gji/ggv035

Nikkhoo, M., Walter, T. R., Lundgren, P. R., & Prats-Iraola, P. (2017). Compound dislocation models (CDMs) for volcano deformation analyses. *Geophysical Journal International*, *208*, 877–894. https://doi.org/10.1093/gji/ggw427

Okada, Y. (1985). Surface deformation due to shear and tensile faults in a half-space. *Bulletin of the Seismological Society of America*, *75*, 1135–1154.

Pelton, J. R., & Smith, R. B. (1979). Recent crustal uplift in Yellowstone National Park. *Science*, *206*, 1179–1182.

Pelton, J. R., & Smith, R. B. (1982). Contemporary vertical surface displacements in Yellowstone National Park. *Journal of Geophysical Research*, *87*, 2745–2761. https://doi.org/10.1029/JB087iB04p02745

Pitt, A. M., Weaver, C. S., & Spence, W. (1979). The Yellowstone Park earthquake of June 30, 1975. *Bulletin of the Seismological Society of America*, *69*, 187–205.

Savage, J. C., Lisowski, M., Prescott, W. H., & Pitt, A. M. (1993). Deformation from 1973 to 1987 in the epicentral area of the 1959 Hebgen Lake, Montana, earthquake (Ms = 7.5). *Journal of Geophysical Research*, *98*, 2145–2153. https://doi.org/10.1029/92JB02410

Smith, R. B., & Braile, L. W. (1994). The Yellowstone hotspot. *Journal of Volcanology and Geothermal Research*, *61*, 121–187. https://doi.org/10.1016/0377-0273(94)90002-7

Tizzani, P., Battaglia, M., Castaldo, R., Pepe, A., Zeni, G., & Lanari, R. (2015). Magma and fluid migration at Yellowstone Caldera in the last three decades inferred from InSAR, leveling, and gravity measurements. *Journal of Geophysical Research: Solid Earth*, *120*, 2627–2647. https://doi.org/10.1002/2014JB011502

Vasco, D. W., Puskas, C. M., Smith, R. B., & Meertens, C. M. (2007). Crustal deformation and source models of the Yellowstone volcanic field from geodetic data. *Journal of Geophysical Research*, *112*, B07402. https://doi.org/10.1029/2006JB004641

Waite, G. P., & Smith, R. B. (2002). Seismic evidence for fluid migration accompanying subsidence of the Yellowstone caldera. *Journal of Geophysical Research*, *107*. https://doi.org/10.1029/2001JB000586

Waite, G. P., & Smith, R. B. (2004). Seismotectonics and stress field of the Yellowstone volcanic plateau from earthquake first-motions and other indicators. *Journal of Geophysical Research*, *109*. https://doi.org/10.1029/2003JB002675

Werner, C., & Brantley, S. (2003). CO_2 emissions from the Yellowstone volcanic system. *Geochemistry, Geophysics, Geosystems*, *4*(7), 1061. https://doi.org/10.1029/2002GC000473

White, D. E., Hutchinson, R. A. & Keith, T. E. C. (1988). The geology and remarkable thermal activity of Norris Geyser Basin, Yellowstone National Park, Wyoming. *U. S. Geological Survey Professional Paper 1456*, 84p, https://pubs.usgs.gov/pp/1456.

Wicks, C., de la Llera, J. C., Lara, L. E., & Lowenstern, J. (2011). The role of dyking and fault control in the rapid onset of eruption at Chaitén volcano, Chile. *Nature*, *479*, 374–378. https://doi.org/10.1038/nature10541

Wicks, C., Weaver, C., Bodin, P., & Sherrod, B. (2013). InSAR evidence for an active shallow thrust fault beneath the city of Spokane Washington, USA. *Journal of Geophysical: Research*, *118*, 1–9. https://doi.org/10.1002/jgrb.50118

Wicks, C. W., Thatcher, W., & Dzurisin, D. (2006). & Svarc. J. (2006). Uplift, thermal unrest, and magma intrusion at Yellowstone Caldera. *Nature*, *440*, 72–75. https://doi.org/10.1038/nature04507

Yang, X.-M., Davis, P. M., & Dieterich, J. H. (1988). Deformation from inflation of a dipping finite prolate spheroid in an elastic half-space as a model for volcanic stressing. *Journal of Geophysical Research*, *93*, 4249–4257.